

**LASER ASSISTED GROWTH OF ZnO  
STRUCTURES IN SELECTED LOCATIONS FOR  
PHOTODETECTORS**

**ABDULWAHAB SALEM ZAROUG LAHEWIL**

**UNIVERSITI SAINS MALAYSIA**

**2023**

**LASER ASSISTED GROWTH OF ZnO  
STRUCTURES IN SELECTED LOCATIONS FOR  
PHOTODETECTORS**

by

**ABDULWAHAB SALEM ZAROUG LAHEWIL**

**Thesis submitted in fulfilment of the requirements  
for the degree of  
Doctor of Philosophy**

**October 2023**

## ACKNOWLEDGEMENT

All praise and thanks are to Allah. Uncountable thanks to my main supervisor, Professor Dr. Naser M. Ahmed, for his guidance and support during the research of my graduate studies. I have been fortunate to work with somebody whose love for research is contagious. I sincerely hope that Prof. Dr. Naser M. Ahmed knows the difference he has made in my career as a graduate student. Above all, I thank him for the great trust he has always placed in me. I am also grateful to my co-supervisor, Dr. Nurul Zahirah Noor Azman, for her kindness and help. She also provided me with the opportunity to conduct research in this field. In particular, I would like to thank Universiti Sains Malaysia and the School of Physics for providing me with the opportunity to pursue this doctoral research. Also, I would like to express my deepest appreciation to the Education Ministry of Tripoli, Libya; the Ministry of Technical & Vocational Education, Tripoli, Libya; and The Institute of Science and Technology of Al-Orban, Libya, for the positive interactions and support. I am also grateful to all of my friends for their academic feedback. This achievement would not have been possible without the love and support of my family. Their sacrifices to provide me with a better life here in Malaysia are now rewarded. Thanks a lot to my parents, wife, children, brothers, and sisters, for being there for me anytime I needed them.

*ABDULWAHAB LAHEWIL*

*Penang-Malaysia March 2023*

## TABLE OF CONTENTS

<b>ACKNOWLEDGEMENT</b> .....	<b>ii</b>
<b>TABLE OF CONTENTS</b> .....	<b>iii</b>
<b>LIST OF TABLES</b> .....	<b>vii</b>
<b>LIST OF FIGURES</b> .....	<b>x</b>
<b>LIST OF SYMBOLS</b> .....	<b>xvi</b>
<b>LIST OF ABBREVIATIONS</b> .....	<b>xviii</b>
<b>ABSTRAK</b> .....	<b>xxi</b>
<b>ABSTRACT</b> .....	<b>xxiii</b>
<b>CHAPTER 1 INTRODUCTION</b> .....	<b>1</b>
1.1 Overview .....	1
1.2 Problem Statement .....	2
1.3 Research Objectives .....	4
1.4 Research Originality.....	4
1.5 Scope of research .....	4
1.6 Thesis outline .....	5
<b>CHAPTER 2 LITERATURE REVIEW</b> .....	<b>6</b>
2.1 Background of ZnO.....	6
2.2 Chemical Methods for Growing ZnO NSs.....	13
2.3 The Advantages of Using Hexamethylenetetramine (HMTA, C <sub>6</sub> H <sub>12</sub> N <sub>4</sub> ) .....	19
2.4 The Advantages of Using Zinc Acetate to Produce the ZnO .....	21
2.5 Continuous Wave of Laser-Assisted Chemical Bath Deposition.....	
Technique for ZnO Nanostructures.....	27
2.6 Development of Semiconductors on Nanostructures Metal Oxide .....	30
2.7 The Metal Buffer Layers and Substrates .....	33
2.8 UV Photodetectors (PDs).....	35

2.9	The Concept of Photodetection.....	35
2.10	MSM UV-Photodetectors.....	37
2.11	Zinc Oxide-Based UV Photodetectors .....	40
2.12	Characteristic Parameters of UV Photodetectors.....	42
2.12.1	Response and Recovery Time.....	43
2.12.2	The responsivity (R).....	45
2.12.3	The Sensitivity (S).....	45
2.12.4	The Current Gain (G).....	45
2.12.5	The Quantum Efficiency ( $\eta$ ).....	46
2.12.6	External Quantum Efficiency (EQE).....	46
2.12.7	Specific Detective ( $D^*$ ).....	46
2.12.8	Noise Equivalent Power (NEP).....	47
<b>CHAPTER 3 METHODOLOGY AND CHARACTERIZATION .....</b>		<b>53</b>
3.1	Introduction .....	53
3.2	Synthesis Technique of ZnO micro-nanostructures.....	53
3.3	Starting Materials.....	55
3.4	Experiment and Preparation of Chemical Bath Solution.....	55
3.5	LACBD with A Flow Solution.....	57
3.6	Laser-assisted chemical bath deposition setup.....	58
3.7	Radio Frequency RF-Sputtering Technique.....	62
3.8	Thermal Annealing Furnace.....	62
3.9	Characterization.....	63
3.10	X-ray diffraction (XRD) .....	64
3.10.1	Peak Broadening Methods for X-ray .....	67
3.11	Field Emission Scanning Electron Microscope (FE-SEM).....	70
3.11.1	Energy-dispersive X-ray spectroscopy (EDXS) .....	71
3.12	Fourier Transform Infrared Spectroscopy (FT-IR).....	73
3.13	UV-VIS-NIR Spectroscopy .....	74
3.14	Electrical Characteristics.....	75

3.15	Summary .....	76
<b>CHAPTER 4 RESULT AND DISCUSSIONS.....</b>		<b>77</b>
4.1	The Effect of Different Metal Buffer Layers and Laser Irradiation Times on the Structural, Morphological and Optical Properties of Zinc Oxide micro-nanorods Using the LACBD Technique.....	77
4.2	Investigating the Structural and Optical Characteristics of ZnO MRs /Ni/ ...	78
4.2.1	Crystallinity Structures Study of ZnO MRs/Ni/glass.....	78
4.2.2	Morphological Study Analysis of ZnO MRs/Ni/glass .....	83
4.2.3	FT-IR Spectra Analysis of ZnO Rs/Ni/glass.....	90
4.2.4	Reflectance Spectra Analysis of ZnO Rs/Ni/glass.....	92
4.3	Investigating the Structural and Optical Characteristics of ZnO Rs/Ti/Glass ... Using the LACBD Method.....	96
4.3.1	Crystallinity Structures Study of ZnO Rs/Ti/glass.....	96
4.3.2	Morphological Study Analysis of ZnO MRs/Ti/glass .....	102
4.3.3	Reflectance Spectra Analysis of ZnO Rs/Ti/glass .....	108
4.3.4	Absorption Spectra Analysis of ZnO Rs/Ti/glass .....	109
4.3.5	Transmittance Spectra Analysis of ZnO Rs/Ti/glass .....	111
4.4	Investigating the Structural and Optical Characteristics of ZnO Rs/Fe/Glass ... Using the LACBD Method.....	116
4.4.1	Crystallinity Structures Study of ZnO MRs/Fe/glass.....	116
4.4.2	Morphological Study Analysis of ZnO MRs/Fe/glass .....	120
4.4.3	FT-IR Spectra Analysis of ZnO MRs/Fe/glass .....	124
4.4.4	Reflectance Spectra Analysis of ZnO MRs/Fe/glass .....	125
4.4.5	Absorption Spectra Analysis of ZnO MRs/Fe/glass .....	126
4.5	Summary .....	130
<b>CHAPTER 5 INVESTIGATING PHOTODETECTOR CHARACTERISTICS FROM ZnO PREPARED BY LACBD WITH DIFFERENT METAL BUFFER LAYERS AND LASER IRRADIATION TIME .....</b>		<b>132</b>
5.1	Introduction .....	132
5.1.1	Photodetector characterization from ZnO prepared with Nickel (Ni) Buffer Layer .....	132

5.1.2.	Fabrication of Photodetectors using Titanium (Ti) Buffer Layer and Different Laser Irradiation Times.....	140
5.1.3	Photodetector Characterization from ZnO Prepared with Fe Buffer Layer.....	144
5.2	Summary .....	149
<b>CHAPTER 6 CONCLUSIONS AND FUTURE RESEARCH .....</b>		<b>154</b>
6.1	Conclusion.....	154
6.2	Future Research.....	156
<b>REFERENCES.....</b>		<b>157</b>
<b>LIST OF PUBLICATIONS</b>		

## LIST OF TABLES

		Page
Table 2.1	Physical properties of the ZnO semiconductor at 300 k [32].....	8
Table 2.2	Comparison of the LACBD synthesis technique in terms of other techniques; the temperature required, synthesis time, grain size, type of zinc source, substrate, and solvent type.....	26
Table 2.3	Summarizes the LACBD and LAFD techniques.....	30
Table 2.4	Shows the electrical nature of ideal metal-semiconductor contact and the present work [112].....	39
Table 2.5	The characteristics of UV pd parameters and their mathematical relationship.....	48
Table 2.6	Summary of key parameters and previous reports thin film photodetectors based on UV-PDs.....	49
Table 4.1	Summarized the peaks from the XRD data of ZnO MRs /Ni/glass correspond to the typical diffraction peaks of hexagonal wurtzite ZnO (ISCD no. 026170 and 024014 for NiO).....	77
Table 4.2	XRD data of ZnO MRs/Ni/glass properties were determined from (002) reflection: full-width half maximum (FWHM) is 0.15°, 0.114° and 0.113°; grain size ( $D$ ); dislocation density ( $\delta$ ); strain ( $\epsilon$ ); stress ( $\sigma$ ); interplanar distance ( $d$ ); lattice constant ( $a$ and $c$ ); positional parameter ( $u$ ); bond length ( $L$ ); and cell volume ( $V$ ), respectively.....	82
Table 4.3	The energy bandgap value of ZnO MRs/Ni/glass/properties are determined from reflectance spectra.....	96
Table 4.4	Summarized the peaks from the XRD data of ZnO MRs/Ti/glass, correspond to the typical diffraction peak of hexagonal wurtzite ZnO ref. cod. 01-075-0576, and 01-071-1166 for TiO <sub>2</sub> .....	97
Table 4.5	XRD data of ZnO MRs/Ti/glass properties were determined from (002) reflection: full width half maximum (FWHM) is 0.25°, 0.10° and 0.25°; grain size ( $D$ ); dislocation density ( $\delta$ ); strain ( $\epsilon$ ); stress ( $\sigma$ ); interplanar distance ( $d$ ); lattice constant ( $a$	

	and $c$ ); positional parameter ( $u$ ); bond length ( $L$ ) and cell volume ( $V$ ), respectively.....	99
Table 4.6	The energy bandgap value of ZnO MRs/Ti/glass properties is determined from transmissions spectra.....	115
Table 4.7	Summarized the peaks from the XRD data of ZnO MRs/Fe/glass correspond to the typical diffraction peaks of hexagonal wurtzite ZnO (ICSD No. Ref. Cod. 01-079-0206 for ZnO, and 00-001-1252 for Fe.....	116
Table 4.8	XRD data of ZnO MRs/Fe/glass properties were determined from (002) reflection: full width half maximum (FWHM) is $0.1184^\circ$ , $0.1184^\circ$ , and $0.1185^\circ$ ; grain size ( $D$ ); dislocation density ( $\delta$ ); strain ( $\epsilon$ ); residual stress ( $\sigma$ ); interplanar distance ( $d$ ); lattice constants ( $a$ and $c$ ); positional parameter ( $u$ ); bond length ( $L$ ); and cell volume ( $V$ ), respectively.....	119
Table 4.9	The energy bandgap value of ZnO MRs/Fe/glass properties are determined from absorbance spectra.....	129
Table 4.10	XRD data of ZnO MRs/Ni/glass, ZnO MRs/Ti/glass, and ZnO MRs/Fe/glass properties were determined from (002) reflection; full width half maximum (FWHM); grain size ( $D$ ); dislocation density ( $\delta$ ); strain ( $\epsilon$ ); residual stress ( $\sigma$ ); interplanar distance ( $d$ ); lattice constants ( $a$ and $c$ ); positional parameter ( $u$ ); bond length ( $L$ ); and cell volume ( $V$ ), respectively.....	131
Table 4.11	The energy bandgap value of ZnO MRs/Ni/glass, Zn MRs/Ti/glass, and ZnO MRs/Fe/properties are determined.....	131
Table 5.1	Under UV 380 nm illumination and a low bias voltage of -5 V, ZnO MRs/Ni/glass SMS photodetectors were measured for rise time ( $\tau_r$ ), recovery time ( $\tau_d$ ), light current ( $I_{light}$ ), dark current ( $I_{dark}$ ), photocurrent ( $I_{photo}$ ), current gain ( $G$ ), photoresponsivity ( $R$ ), photosensitivity ( $S$ ), quantum efficiency ( $\eta$ ), specific detectivity ( $D^*$ ), noise equivalent power (NEP), and external quantum efficiency (EQE).....	139

Table 5.2	The electrical characteristics of rise time ( $\tau_r$ ), recovery time ( $\tau_d$ ), light current ( $I_{\text{light}}$ ), dark current ( $I_{\text{dark}}$ ), photocurrent ( $I_{\text{photo}}$ ), current gain (G), photoresponsivity (R), photosensitivity (S), quantum efficiency ( $\eta$ ), specific declivity ( $D^*$ ), noise equivalent power (NEP), and external quantum efficiency (EQE) of photodetectors prepared using the LACBD technique of ZnO MRs/Ti/glass at different laser irradiation times of 20, 25, and 30 minutes, respectively.....	143
Table 5.3	The calculated values of rise time ( $\tau_r$ ), recovery time ( $\tau_d$ ), light current ( $I_{\text{light}}$ ), dark current ( $I_{\text{dark}}$ ), photocurrent ( $I_{\text{photo}}$ ), current gain (G), photoresponsivity I, photosensitivity (S), quantum efficiency ( $\eta$ ), specific declivity ( $D^*$ ), noise equivalent power (NEP), and external quantum efficiency (EQE) of ZnO MRs/Fe/glass device photodetector prepared on laser irradiation times of 20, 25, and 30 minutes.....	148
Table 5.4	Compression of optimal PDs properties comparison of optimal PDs properties prepared at different metal buffer layers of nickel, titanium, and iron with 25 minutes of laser irradiation time, a UV light wavelength of 380 nm, and a bias voltage of -5 volts with other studies.....	152

## LIST OF FIGURES

		<b>Page</b>
Figure 2.1	Semiconductor ZnO crystallizes in two main forms: hexagonal wurtzite and cubic zinc blend. Wurtzite (a) Zn and O are grey and yellow atoms, and zinc blende (b) Zn and O are blue and yellow atoms, respectively [30] .....	7
Figure 2.2	Shows different synthesis techniques of ZnO morphologies are produced by: (a), (b), and (c) chemical bath deposition [4]; (d), (e) and (f) electrodeposition [5] [6] Hydrothermal/solvothermal synthesis (g), (h) and (i), electrospinning (j) and (k) and laser-assisted flow deposition (l) [4] [6] [7] [8].....	9
Figure 2.3	Shows (a) ZnO UV sensor growth on tracing (b) Whatman paper Transparent UV sensor development on a glass substrate, and (c) UV sensor growth on a paper substrate with ZnO nanowires over graphite electrodes [44].....	11
Figure 2.4	Shows (a) a schematic of a ZnO photodetector manufactured by flame spray pyrolysis and (b) a Photographic image of a ZnO UV sensor Bluetooth-connected to a smartphone displaying photocurrent variation during UV radiation on/off cycles [44].....	12
Figure 2.5	SEM images of the ZnO balls show, (a) ball-shaped nanorod structure in three dimensions as subsequent nanorods grow in all directions, (b) growth of newly generated nanorods along their own c-axis, as well as the nucleation and growth of rods from the joint section of the original structure, and (c) many ball-shaped nanorod structures [48] [47].....	13
Figure 2.6	The energy band diagram in a semiconductor and the method of charge carrier production by photoexcitation [110].....	36
Figure 2.7	Schematic the mechanism of a photodetection process [111]....	37

Figure 3.1	The methodology and fabrication methods for ZnO micro-nanostructures, as well as the schematic of buffer layer electrodes and the ZnO/glass photodetector design, are depicted in the flow chart.....	54
Figure 3.2	(a)1. raw glass substrate, (a)2. glass substrate with slot, and (a)3. glass substrate with laser spot, (b) show only the cavity, (c) show the cavity with laser spot, (d and e) the system approach for ZnO micro-nanostructures using the LACBD technique.....	56
Figure 3.3	Shows the preparation of the system: (a) the power meter source device to measure the incident power of UV light, (b) the deposition system using the laser-assisted chemical bath deposition technique (LACBD), and (c) shows the sample inside the bottle immersed in the solution and (d) an FE-SEM top view image of ZnO MRs deposited on different metal buffer layers.....	60
Figure 3.4	Shows the Auto HHV500 RF-sputtering system image (a), and schematic diagram of the RF-sputtering image (b).....	62
Figure 3.5	Shows (a) an annealing tube furnace (model Lenton VTF/12/60/700), and (b) a thermal tube furnace (schematic).....	63
Figure 3.6	Shows (a) the X-ray diffractometer (XRD), the D8 Advance X-ray diffractometer from Bruker AXS, and (b) shows the schematic design employed.....	65
Figure 3.7	Geometric representation of the Bragg Law, interferences caused by the $2\theta$ deviation as constructive (left) or destructive (right).....	66
Figure 3.8	Shows (a) a Photograph of a Field Emission Scanning Electron Microscopy (FE-SEM) System, and (b) Electron Optic Column Design for FE-SEM [161].....	71
Figure 3.9	Shows the signals produced during the interaction of the electron beams with the surface of the sample during FE-SEM imaging [161].....	72

Figure 3.10	Shows the FT-IR spectrometer system, and the inset image shows the crystal and arm design attachments.....	73
Figure 3.11	Shows the image of Agilent Technologies Cary 5000 UV-Vis NIR spectrophotometer.....	74
Figure 3.12	Shows the Photodetector testing setup.....	75
Figure 4.1	Shows the XRD results of ZnO MRs/Ni/glass thin films using LACBD technique at different laser irradiation times of 20, 25 and 30 minutes, as well as post-annealing at 400 °C for 3 hours, respectively.....	79
Figure 4.2	Shows (a) the FE-SEM top view and (b), (c) and (d) at different magnification images of the ZnO MRs/Ni/glass thin film that was prepared a year ago and stored in a container at room temperature, the same sample was re-examined again after a year using the laser irradiation time of 20 minutes.....	84
Figure 4.3	Shows the FE-SEM top view (a), and the laser irradiation times (S1, b-d,) of 20, (S2, b-d) of 25 and (S3, b-d) of 30 minutes at different magnification images and EDX spectra of ZnO/Ni/glass thin films using LACBD technique, as well as post-annealing at 400 °C for 3 hours, respectively.....	88
Figure 4.4	Shows the FT-IR spectra of ZnO MRs/Ni/glass thin films using LACBD technique at different laser irradiation times (a) 20, (b) 25, and (c) 30 minutes as well as post-annealing at 400 °C for 3 hours respectively.....	91
Figure 4.5	Shows the optical reflectance spectra of ZnO MRs/Ni/glass thin films using LACBD technique at different laser irradiation times of (a) 20, (b) 25 and (c) 30 minutes as well as post-annealing at 400 °C for 3 hours respectively.....	93
Figure 4.6	Shows the Plots of $(\alpha h\nu)^2$ vs. photon energy of ZnO MRs/Ni/glass thin films using LACBD technique at different laser irradiation times of (a) 20, (b) 25 and (c) 30 minutes as well as post-annealing at 400 °C for 3 hours respectively.....	95

Figure 4.7	Shows the XRD results of ZnO MRs/Ti/glass thin films using LACDB technique at different laser irradiation times (a) 20, (b) 25 and (c) 30 minutes as well as post-annealing at 400 °C for 3 hours respectively.....	98
Figure 4.8	Shows the FE-SEM top view at different magnification images and EDX spectra of ZnO MRs/Ti/glass thin films using LACBD technique of laser irradiation times of (S1, a-d) 20, (S2, a-d) 25 and (S3 a-d) 30 minutes as well as post-annealing at 400 °C for 3 hours respectively.....	107
Figure 4.9	Shows the reflectance spectra of ZnO MRs/Ti/glass thin films using the LACBD technique of laser irradiation times of 20, 25 and 30 minutes as well as post-annealing at 400 °C for 3 hours respectively.....	109
Figure 4.10	Shows the optical absorbance spectra of ZnO MRs/Ti/glass thin films using LACBD technique at different laser irradiation times of (a) 20, (b) 25 and (c) 30 minutes, as well as post-annealing at 400 °C for hours respectively.....	110
Figure 4.11	Shows the optical transmittance spectra of ZnO MRs/Ti/glass thin films, using the LACBD technique as well as post-annealing at 400 °C for 3h at different irradiation times of (a) 20, (b) 25 and (c) 30 minutes respectively.....	112
Figure 4.12	Shows the variation of $(\alpha h\nu)^2$ against applied energy ( $h\nu$ ) of the ZnO MRs/Ti/glass thin films using LACBD technique as well as post-annealing at 400 °C for 3 hours at different laser irradiation times of (a) 20, (b) 25 and (c) 30 minutes respectively.....	114
Figure 4.13	Shows the XRD results of ZnO MRs/Fe/glass thin films using LACBD technique as well as post-annealing at 400 °C for 3 hours at different laser irradiation times of (a) 20, (b) 25, and (c) 30 minutes respectively.....	117

Figure 4.14	Shows the FE-SEM top view, different magnification images and EDX spectra of ZnO MRs/Fe/ glass thin films using LACBD technique as well as post-annealing at 400 °C for 3 hours at different laser irradiation times of (S1, a-d) 20, (S2, a-d) 25, and (S3, a-d) 30 minutes respectively.....	123
Figure 4.15	Shows the FT-IR spectra of ZnO MRs/Fe/glass thin films using LACBD technique as well as post-annealing at 400 °C for 3 hours at different laser irradiation times of (a) 20, (b) 25, and (c) 30 minutes, respectively.....	125
Figure 4.16	Shows the UV-vis reflectance spectra of ZnO MRs/Fe/glass thin films using LACBD technique as well as post-annealing at 400 °C for 3 hours at different laser irradiation times of (a) 20, (b) 25 and (c) 30 minutes, respectively.....	126
Figure 4.17	Shows the UV-vis absorption spectra of the ZnO MRs / Fe / glass thin films using LACBD technique as well as post-annealing at 400 °C for 3 hours at different laser irradiation times of (a) 20, (b) 25, and (c) 30 minutes, respectively.....	127
Figure 4.18	Shows the energy bandgap plot of ZnO MRs/Fe/glass thin films using LACBD technique as well as post-annealing at 400 °C for 3 hours at different irradiation times of (a) 20, (b) 25, and (c) 30 minutes respectively.....	129
Figure 5.1	Shows the I-V characteristics, response, and recovery time of the repeatability property (on/off) of ZnO MRs / Ni / glass photodetectors under UV illumination (= 380 nm, 0.7186 mW/cm <sup>2</sup> ) and low applied bias voltages of (-5V) for three different samples prepared at laser irradiation times (a) 20, (b) 25, and (c) 30 minutes, respectively.....	138
Figure 5.2	Shows the I-V characteristics, response, and recovery time of the repeatability property (on/off) of the ZnO MRs/Ti/glass photodetectors under pulsed UV light (380 nm, 0.7186 mW/cm <sup>2</sup> ) at low applied bias voltages of (-5 V), for three different laser irradiation times of (a) 20, (b) 25, and (c) 30 minutes respectively.....	142

Figure 5.3 Shows the I-V characteristics, response, and recovery time of the repeatability property (on/off) of ZnO MRs/Fe photodetectors at low applied bias voltage (-5 V) for three different samples prepared at laser irradiation times (a) 20, (b), 25, and (c) 30 minutes, respectively..... 147

## LIST OF SYMBOLS

$\beta_{hkl}$	Instrument-corrected full width at half maximum
$\sigma$	Strain
$\delta$	Dislocation density
$\eta$	Quantum efficiency
$\theta$	Theta
$\lambda$	Wavelength
$\tau_d$	Recovery time
$\tau_r$	Rise time
$^{\circ}\text{C}$	Celsius temperature
$h\nu$	Vibrational phonon energy
$\theta_{hkl}$	Diffraction peak position
$\Phi$	Work function
$\Phi_M$	Metal work function
$\Phi_S$	Semiconductor work function
$a$ and $c$	Lattice constant
$D$	Grain size
$D^*$	Specific detectivity
$d$	Interplaner distance
$E$	Energy of photon

e	Charge of electron
EV	Valence band energy
G	Gain
h	Planck's constant
I-V	Current and voltage
R	Photoresponsivity
S	Sensitivity
s	Second
t	Time

## LIST OF ABBREVIATIONS

1D	One dimensional
2D	Two dimensional
3D	Three dimensional
Ae-	Auger electrons
AFM	Atomic force microscopy
Al	Aluminium
ALD	Atomic laser deposition
BSE	Backscattering electron
CBD	Chemical bath deposition
CVD	chemical vapor deposition
DSSCS	Day-sensitized solar cells
EC	Conduction band energy
EDXS	Energy-dispersive X-ray spectroscopy
EQE	External quantum efficiency
Fe	Iron
FE-SEM	Field emission scanning electron microscopy
FTIR	Fourier transform infrared spectroscopy
HCP	hexagonal close-packed
LACBD	Laser assisted chemical bath deposition

LED	Light emitting diode
MRs	Microrods
MSM	Metal semiconductor metal
M/L	Mol per litter
NBE	Near band edge
NEP	Noise equivalent power
nm	Nanometer
Ni	Nickel
NPs	Nanoparticles
NSs	Nanostructures
NRs	Nanorods
NWs	Nanowires
Pd	palladium
PL	Photoluminescence
PLD	Pulsed laser deposition
QDs	Quantum dots
Rf sputtering	Radio frequency magnetron sputtering
Se-	Secondary electron
SILAR	Successive ionic layer adsorption and reaction
SPS	Spray pyrolysis synthesis
Ti	Titanium

UV-vis	Ultraviolet emission
μm	micrometer
VPT	Vapour phase transport
XRD	X-ray diffraction
XPS	X-ray photoelectron spectroscopy
ZnO	Zinc oxide

## **PERTUMBUHAN STRUKTUR ZnO DENGAN BANTUAN LASER DI LOKASI TERPILIH UNTUK PENGESAN FOTO**

### **ABSTRAK**

Ciri-ciri luar biasa zink oksida (ZnO) satu dimensi merupakan bahan yang berpotensi tinggi untuk pelbagai aplikasi peranti elektrik, elektrokimia, elektromekanikal dan pengesanan. Pada pelbagai tempoh penyinaran laser berterusan selama 20 minit, 25 minit dan 30 minit, kaedah pemendapan rendaman kimia berbantuan laser (LACBD) yang mudah dan cepat telah digunakan pada substrat kaca diikuti proses pasca penyepuhlindapan selama tiga jam pada suhu 400°C. Struktur ZnO berfungsi yang dikenali sebagai mikro-nanorod dengan ciri struktur, morfologi dan optik yang berkualiti telah ditumbuhkan pada substrat kaca yang disaluti dengan lapisan penimbal logam berbeza iaitu nikel (Ni) dan titanium (Ti) menggunakan kaedah percikan frekuensi radio (RF) manakala ferum (Fe) melalui kaedah penyejatan haba. Variasi dalam analisis morfologi, kehabluran, komposisi kimia serta spektrum pemantulan, penyerapan dan penghantaran optik masing-masing telah disiasat, dibincangkan dan dikaitkan dengan perubahan terhadap tempoh penyinaran laser. Pola XRD menunjukkan bahawa bahan yang disintesis mempunyai puncak ZnO MRs (002) yang tinggi, struktur wurtzit berbentuk heksagon serta mempamerkan orientasi pilihan sepanjang orientasi paksi-c bagi semua sampel. Saiz butiran kristal telah meningkat dan masing-masing didapati berada dalam julat antara 8.88 nm hingga 12.16 nm bagi sampel yang menggunakan lapisan Ni, 4.772 nm hingga 11.955 nm bagi sampel yang menggunakan lapisan Ti dan 11.699 nm bagi sampel yang menggunakan lapisan penimbal ferum (Fe). Analisis penyebaran tenaga sinar-X (EDX) telah digunakan untuk mengenal pasti komponen-komponen terlibat dan mengesahkan komposisi

bahan kimia yang diperlukan terbukti wujud. Jurang jalur tenaga ( $E_g$ ) masing-masing telah ditentukan dengan nilai 3.35, 3.36, 3.31, and 4.12, 4.23, 4.16; and 3.22, 3.06, and 3.03 eV. Ciri-ciri elektrik bagi ZnO NRs telah ditentukan menggunakan meter sumber siri Keithley 2400 berkadar 20W. Ia digunakan bagi menguji sifat elektrik fotopengesan UV termasuk arus cahaya ( $I_{light}$ ), arus gelap ( $I_{dark}$ ), fotoarus ( $I_{ph}$ ), gandaan arus ( $G$ ), fotokepekaan ( $S_{ph}$ ), kecekapan kuantum ( $\eta$ ), fotoresponsif ( $R$ ), masa naik ( $\tau_r$ ), masa pemulihan ( $\tau_d$ ), pengesanan khusus ( $D^*$ ), kuasa setara hingar (NEP) dan kecekapan kuantum luaran (EQE), berasakan peranti MSM PD. Pengukuran telah diambil dalam kegelapan sepenuhnya, dengan menggunakan cahaya UV yang mempunyai panjang gelombang sebanyak 380 nm dan keamatan kuasa cahaya yang menyinari PD sebanyak  $0.7186 \text{ mW/mm}^2$ . Hasil kajian menunjukkan bahawa penggunaan lapisan penimbal logam yang berbeza iaitu Ni, Ti dan Fe memainkan peranan penting kepada orientasi pertumbuhan dan kadar pertumbuhan ZnO MRs. Tambahan pula, hasil kajian menunjukkan bahawa penyinaran laser telah mengubah struktur permukaan dan ciri topografi filem-filem nipis polihabluran ZnO MRs secara efisien. Lapisan penimbal logam terbaik adalah Ti dengan tempoh penyinaran laser selama 25 minit. Menurut dapatan kajian, PD berasakan MRs tersebut menunjukkan kestabilan dan tindak balas yang luar biasa dalam kedua-dua keadaan gelap dan terang. Penyelidikan ini penting untuk meningkatkan fungsi optoelektronik berasakan ZnO menggunakan kaedah LACBD yang cepat dan mudah.

# LASER ASSISTED GROWTH OF ZnO STRUCTURES IN SELECTED LOCATIONS FOR PHOTODETECTORS

## ABSTRACT

The exceptional characteristics of one-dimensional zinc oxide (ZnO), which has applications in electrical, electrochemical, electromechanical, and sensing devices, make it one of the most promising nanostructures. At various continuous laser irradiation times of 20, 25, and 30 minutes, respectively, utilizing a simple and quick laser-assisted chemical bath deposition (LACBD) method on glass substrates with a three-hours post-annealing at 400 °C. Functional ZnO nanostructures known as micro-nanorods with satisfactory structural, morphological, and optical properties were grown on a glass substrate coated with various metal buffer layers of nickel (Ni), titanium (Ti), using RF sputtering, and iron (Fe), using thermal evaporation. Variation in morphology analysis, crystallinity, and the optical spectra of reflectance, absorption, and transmission have been investigated, discussed, and connected with changes in laser irradiation periods, respectively. The XRD patterns showed that the synthesized material had a strong ZnO MRs (002) peak, a hexagonal wurtzite structure, and exhibited a preferred orientation along with the *c*-axis orientation for all the samples. The crystallite grain size increased and was found to be in the range of 8.88 nm to 12.16 nm for the samples using Ni, 4.772 nm to 11.955 nm for the samples using Ti, and 11.699 nm for the samples using Fe buffer layers, respectively. The energy-dispersive X-ray (EDX) analysis was used to identify the components and confirm that the required composition was present. The energy bandgap ( $E_g$ ) for different metal buffer materials, nickel, titanium, and iron, at different laser irradiation times of 20, 25, and 30 minutes was determined to be 3.35, 3.36, 3.31, 4.12, 4.23, 4.16, 3.22, 3.06,

and 3.03 eV, respectively. The electrical characteristics of ZnO MRs were also determined and used to test the electrical properties of the UV photodetectors, including light current ( $I_{\text{light}}$ ), dark current ( $I_{\text{dark}}$ ), photocurrent ( $I_{\text{ph}}$ ), current gain (G), photosensitivity ( $S_{\text{ph}}$ ), quantum efficiency ( $\eta$ ), photoresponsivity (R), rise time ( $\tau_r$ ), recovery time ( $\tau_d$ ), specific detectivity ( $D^*$ ), noise equivalent power (NEP), and external quantum efficiency (EQE), based on MSM PD devices. The results show that using different metal buffer layers of Ni, Ti, and Fe plays an essential role in the growth orientation and growth rate of the ZnO MRs. Additionally, the results showed that the laser irradiation substantially changed the surface structures and topographic characteristics of the polycrystalline ZnO MRs thin films. The best metal buffer layer was Ti with 25 minutes of laser irradiation. According to our findings, in both dark and light circumstances, the MRs-based PD provides exceptional stability and responsiveness. This research is important for increasing the functioning of ZnO-based optoelectronics using a quick and easy LACBD approach.

## CHAPTER 1 INTRODUCTION

### 1.1 Overview

There is a lot of research on the growth and characterization of one-dimensional nanostructures of elemental and composite semiconductors such as silicon (Si), germanium (Ge), indium phosphide (InP), gallium arsenide (GaAs), and zinc oxide (ZnO). ZnO is a nontoxic and abundant material with electrical, optical, chemical, and mechanical characteristics that make it very suitable for a diversity of applications in optoelectronics, sensors, and solar cells. At room temperature, the arranged positive exciton binding energy (60 meV) is much higher than that of ZnS (20 meV) and GaN (21 meV) [1]. ZnO is a well-known n-type semiconductor with distinguishing characteristics such as a 3.37 eV bandgap [2][3] and high electron mobility ( $100 \text{ cm}^2\text{V}^{-1}\text{s}$ ) [4]. The extraordinary features of the ZnO semiconductor material, notably its high optical gain, have drawn worldwide interest during the previous century. According to recent studies, nanostructured ZnO is being investigated intensively because of its capabilities with remarkable structural, optical, and electrical properties. The achievement of controlling the growth of the surface of nanostructures like ZnO has significant applications. Huge approaches have been studied to create ZnO nanostructure materials, like pulsed laser deposition (PLD) [5], sol-gel method, [6], [7] chemical bath deposition (CBD) [8][9], and laser-assisted chemical bath deposition (LACBD) [10]–[14]. Overall, the average grain size determined by the LACBD method is related to the average diameter of the micro-nanostructured ZnO as laser irradiation period is increased. Several types of buffer layers are created from ZnO using RF sputtering [15], electrochemical deposition [16],

successive ionic layer adsorption and reaction (SILAR) [17], [18], and metalorganic CVD, ZnO: Ga (GZO) and ZnO: Al (AZO) layers [19].

The simple catalyst-free hydrothermal technique was used to fabricate ZnO NRs at a low temperature of less than 100 °C on a glass substrate coated with various seed layers of Ni and Pd, respectively. Studies have been done on the impact of post-annealing at 400 °C for three hours on thin films (TFs), ZnO NRs surface morphology, and crystallinity. Investigations have also been done into the effects of laser exposure time [20].

This study's main objective is to find out how different laser irradiation times of 20 minutes, 25 minutes, and 30 minutes affect the structural, morphological, optical, and electrical characteristics of ZnO nanostructures. Moreover, the metal buffer layers of Ni, Ti, and Fe on glass substrates are used in this study.

## **1.2 Problem Statement**

The main difficulties slowing the advance of ZnO nanostructure research are the poor realization and control of surface growth and the lack of scale in the correlation between the obtained morphology and growth parameters. The issue of repeatability of nanostructure parameters, which includes nano ZnO, is the fundamental barrier to the manufacturing and use of many types of nanostructures [21].

By adding a second external energy source to the process, the modified CBD is a novel method that modifies the optoelectronic properties of thin films. LACBD method is a promising approach to achieve this at low temperatures and in extremely small regions measuring hundreds of micrometres, and the structures formed are of good quality. The LACBD method for regulating the crystalline surface structures of ZnO NRs relies heavily on growing time. More  $Zn^{+2}$  and  $O^{2-}$  may combine into the

ZnO lattice as growing time increases, changing ZnO's structural and morphological features [22][23]. Only 3mL of the solution was used to fabricate and synthesize the MSM photodetector's active region. Both methods are used for thin-film deposition in various applications, including electronics, photonics, and photovoltaics. Each method has its own set of advantages and limitations. LACBD offers certain advantages over traditional CBD in terms of improved control and potentially enhanced film properties. However, it also introduces complexities and may not be universally applicable, depending on the specific material and application requirements. The choice between CBD and LACBD should be based on the desired film properties, substrate compatibility, and available resources.

To avoid losing electrons and holes by recombination, reduce the active area to achieve quick conduction of electrons and holes to electrodes before recombination. Because of the growth of small grains and areas using LACBD technology, the photodetector can be created at a tiny size with high efficiency, which prevents electron-hole pairs from recombination in the ZnO/metal/glass MSM composite [9]. After achieving high-quality structures and very small areas using the LACBD method, we measured the photodetector obtained with different metal buffer layers and different laser irradiation times with an appropriate metal work function to obtain Ohmic curves with high efficiency. Deep studies on the electrical properties, and the greatest results were found when using titanium buffer layers at 25 minutes of laser irradiation time.

### **1.3 Research Objectives**

The research development uses the following specific objectives:

1. To study synthesizing ZnO nanostructure in very small, selected areas on the top of a metal/glass substrate by using the laser-assisted chemical bath deposition (LACBD) technique.
2. To examine the effect of the metal buffer layer on the glass substrates for the ZnO structure using different laser irradiation times of 20, 25, and 30 minutes.
3. To investigate micro-nanostructure active areas for photodetector applications with high efficiency.

### **1.4 Research Originality**

This work's uniqueness is defined by the following characteristics:

- 1- New ZnO nanostructures on various metals were synthesized using the LACBD technique.
- 2- New technique to fabricate UV photodetector with very small area micro-nano areas for fast response MSM PDs using ZnO NSs.

### **1.5 Scope of research**

ZnO micro-nanorods were created on glass substrates coated with various metal buffer layers such as nickel (Ni), titanium (Ti), and iron (Fe) using laser-assisted chemical bath deposition (LACBD) method. From recent research, the optimal chemical ZnO MRs concentration was used to design and manufacture several MSM UV PD devices with ZnO MRs samples. At different laser irradiation periods of 20, 25, and 30 minutes, respectively, the settings were tuned to control the crystal structure, surface morphology, optical, and electrical characteristics of ZnO MRs. Improvements and adequate quality in the synthesis technique of ZnO MRs at various metal buffer layers may be generated.

## **1.6 Thesis outline**

The thesis is outlined as follows.

Chapter 1; Has a brief introduction to zinc oxide (ZnO) on various metal buffer layers. The problem statement, research objectives, and significance are also highlighted, as are the originality of the research and the scope of the study.

Chapter 2; The literature gives a brief history of the use of zinc oxide in laser-assisted chemical bath deposition and discusses how to make unique PDs.

Chapter 3; This chapter shows the research methodology, experimental work, and equipment used in this research.

Chapter 4; This chapter focuses on the results and discussion for the different three prepared samples characterized using XRD, FE-SEM, EDX, FT-IR, and UV-vis spectroscopy.

Chapter 5; The chapter shows the electrical characterization of the ZnO MSs/metal buffer layer/glass (MSM) PD devices on different metals. By using the laser-assisted chemical bath deposition (LACBD) technique.

Finally, Chapter 6; presents the conclusion and suggestions for further study.

## CHAPTER 2 LITERATURE REVIEW

### 2.1 Background of ZnO

Zinc oxide has been investigated intensively since 1935 because of its use in a variety of applications, with a particular focus on ZnO-based electrical and optoelectronic devices. At ambient temperature, ZnO is an n-type semiconductor with a large exciton binding energy of 60 meV and a wide bandgap of 3.2 to 3.4 eV. At room temperature and pressure, ZnO crystallizes in the hexagonal wurtzite form, with each anion surrounded by four cations at the corner of a tetrahedron. Other structures, such as "zinc mix" (a phrase derived from compounds like ZnS, which can have cubic or hexagonal phases) or "rock salt" (which contains a cubic phase), may arise, but they are not stable phases under ambient conditions [24]. The unit cell in the hexagonal wurtzite phase of ZnO's crystal structure (P63mc space group) has lattice constants of ( $a = 0.3296$  nm and  $c = 0.52065$  nm) [2], and its ratio of  $c/a$  is 1.602 [25]. The presence of two interconnected sublattices of  $\text{Zn}^{2+}$  and  $\text{O}^{2-}$  ions in which each zinc ion is surrounded by a tetrahedron of four oxygen ions characterizes the ZnO space group. Along the  $c$ -axis, the zinc and oxygen ions alternately form positive and negative polar planes that are abundant in  $\text{Zn}^{2+}$  and  $\text{O}^{2-}$ , respectively. The origin of polar symmetry along the hexagonal axis is the  $\text{Zn}^{2+}$  and  $\text{O}^{2-}$  tetrahedral coordination [26]. The anisotropic development of 1D ZnO crystallites causes this asymmetry along the  $c$ -axis. The most typical and stable ZnO crystal has a wurtzite structure with four face terminations: (0001) polar Zn terminated, and O terminated (0001) facets, as well as a wurtzite structure with four face terminations and the non-polar (1010),

faces [27], [28], an equal number of Zn and O atoms. Figure 2.1 illustrate an atomic model of the polar and non-polar facets of the ZnO hexagonal wurtzite structure, as well as a schematic representation of the facets [29]. Table 2.1 summarizes the physical properties of ZnO.

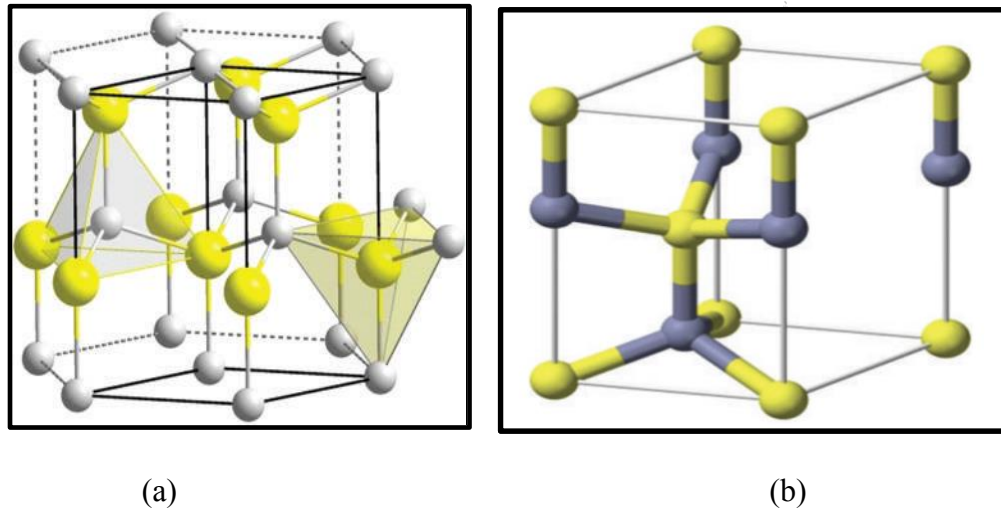


Figure 2.1 Semiconductor ZnO crystallizes in two main forms: hexagonal wurtzite and cubic zinc blende. Wurtzite (a) Zn and O are grey and yellow atoms, and zinc blende (b) Zn and O are blue and yellow atoms, respectively [30].

Nonpolar facets have different chemical and physical characteristics from polar facets, whereas polar facets with an O-terminus have a slightly different electronic structure. These properties are responsible for ZnO's diverse capabilities, such as piezoelectricity and spontaneous polarization, as well as playing an important role in crystal formation and defect generation. When used in gas sensing or other applications, the polar Zn-terminated (0001) facets are more polar than the O-terminated (0001) and non-polar (1010) facets [31].

Table 2.1 Physical properties of the ZnO semiconductor at 300 k [32].

Property	Value
Lattice parameters ( $a, c$ )	0.32495 nm, 0.52069 nm
Energy band gap	3.4 eV (direct)
Exciton binding energy	60 meV
Density	5.606 g/cm <sup>3</sup>
Stable phase at 300k	wurtzite
Refractive index	2.008
Dielectric constant	8.66
Intrinsic carrier concentration (cm <sup>-3</sup> )	~ 10 <sup>6</sup> cm <sup>-3</sup>
Melting point	1975 °C

By using both conventional and microwave-assisted heating, ZnO nanostructures can be created by chemical bath deposition (CBD), electrospinning, electrodeposition, laser-assisted flow deposition (LAFD), and hydrothermal/solvothermal synthesis [27][33][34]. because there is a lot of OH that sticks to the inefficiently coordinated Zn sites, resulting in extremely active facets [25][35][36]. Figure 2.2 shows that Zinc oxide can have a variety of nanostructures, such as nanorods, nanofibers, nanoneedles, nanowires, nanoplates, nanostars, tetrapods, and nanoflowers, depending on the synthesis technique, precursors utilized and their concentrations, solution pH, or even the solvents used [33].

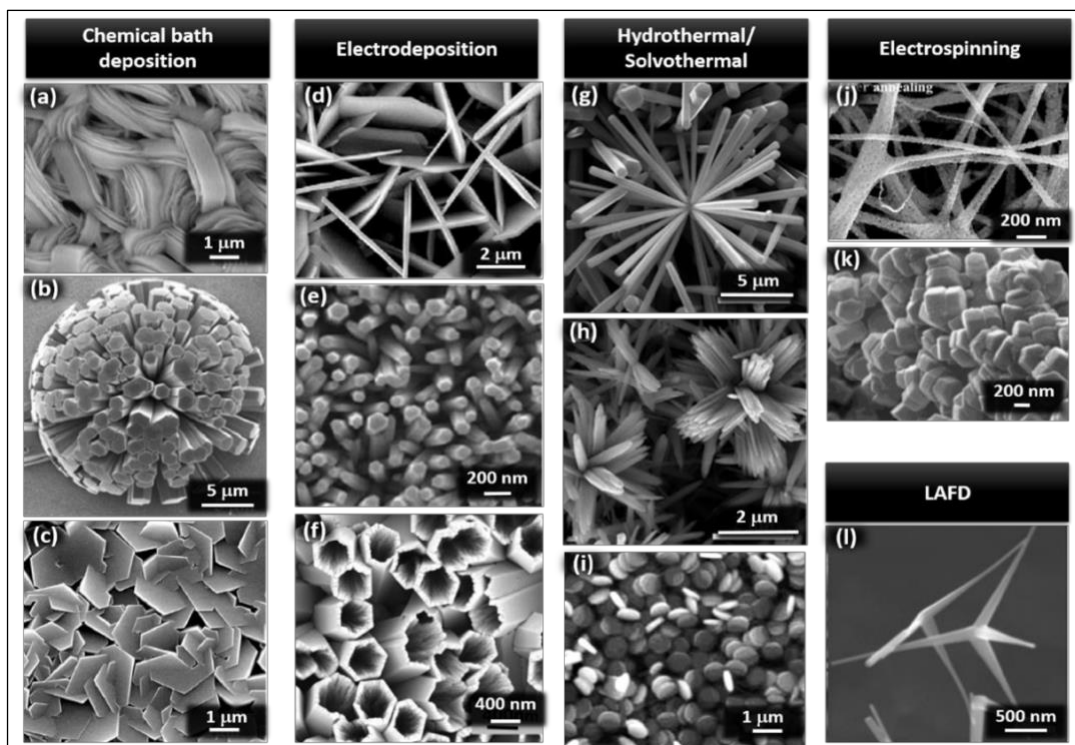


Figure 2.2 Shows different synthesis techniques of ZnO morphologies are produced by: (a), (b), and (c) chemical bath deposition [4]; (d), (e) and (f) electrodeposition [5] [6] Hydrothermal/solvothermal synthesis (g), (h) and (i), electrospinning (j) and (k) and laser-assisted flow deposition (l) [4, 6, 7, 8].

UV photoresponse of ZnO material was discovered in the 1950s [37]. Since then, zinc oxide has been one of the most researched metal oxide compounds for UV sensor applications. Initially, researchers concentrated their efforts on developing ZnO thin film-based sensors. On the other hand, these films have some inherent flaws, such as slow response times and recovery speeds. As a result, numerous authors have documented the use of ZnO nanostructures (such as nanorods, nanostars, and tetrapods) to increase photoresponse time by increasing sensor surface area since 2001 [38]. Because the

photoresponse of ZnO is related to the adsorption and desorption of chemisorbed oxygen from (0001) polar facets, the use of 1D nanostructures has some advantages due to their large surface-to-volume ratio, which allows for an increase in the sensor's photoresponse and a reduction in the active area (both of which are important for device miniaturization) [39][40].

The substrate, ZnO particle shape, and even sensor architecture are all factors that can affect the sensitivity of a ZnO UV sensor. Alenezi et al. created a series of flexible sensors with various designs that displayed varying photocurrent response values and used a bridge nanosizing setup to boost sensitivity while maintaining a rapid response time (90 ms) and recovery time (210 ms) [41]. Pimentel et al. demonstrated the manufacture of ZnO UV sensors on rigid or flexible substrates (glass or PET/PEN) as well as substrates made of cellulosic materials [42]. The ZnO UV sensors constructed on glass and cellulosic substrates are depicted in Figure 2.3.

The low photocurrent value of ZnO micro-nanostructures in the UV is a drawback, owing to the small size of individual nanowires. Researchers are experimenting with various approaches to improve the photoresponse of ZnO UV photodetectors. The difference between employing ZnO nanowires positioned horizontally along the substrate and using the identical nanowires set vertically against the substrate was demonstrated. The performance of the flexible and rigid sensors was comparable, with on/off current ratios that were roughly three orders of magnitude higher than those of polycrystalline ZnO thin film sensors. Photoresponse currents and on/off current ratios for the rigid and flexible UV sensors reached 12.22 mA and 82 000, and 14.1 mA and 120 000, respectively, at UV irradiance of 4.5 mW/cm<sup>2</sup> and 3 V bias [43].

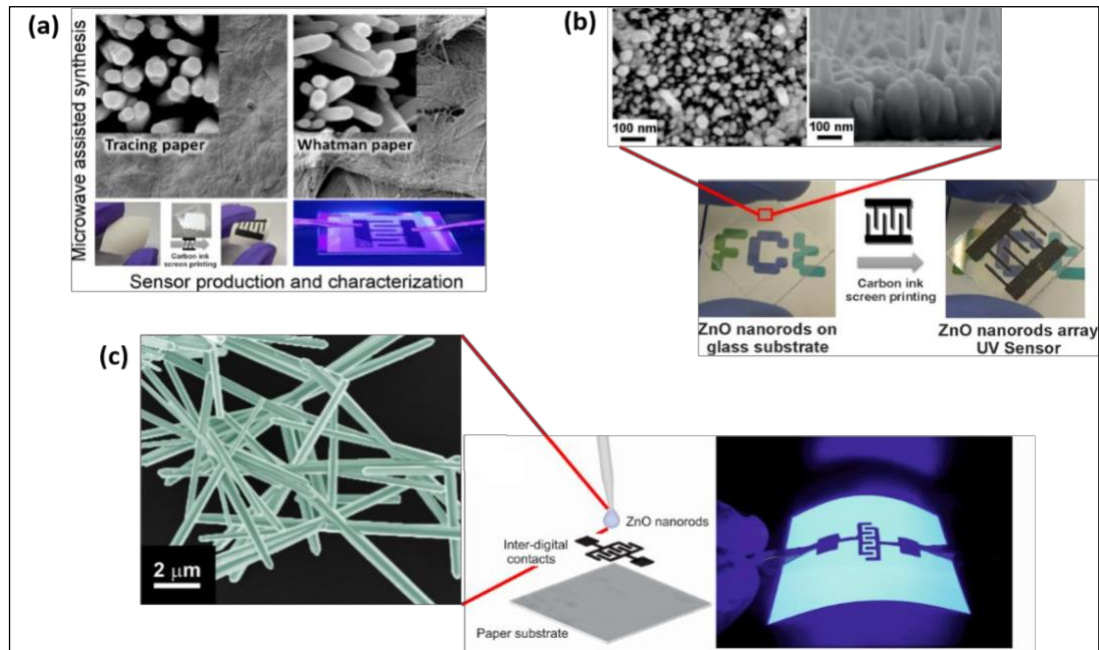


Figure 2.3 Shows (a) ZnO UV sensor growth on tracing, (b) Whatman paper transparent UV sensor development on a glass substrate, and (c) UV sensor grown on a paper substrate with ZnO nanowires over graphite electrodes [44].

Spray flame synthesis was used to produce ZnO nanoparticles with a diameter of 19 nm [45] see Figure 2.4 (a). The ultra-porous ZnO nanoparticle coating, which presents an increased photocurrent from 260  $\mu\text{A}$  to 1.2 mA, contributes to the sensor's high sensitivity. provide another highly interesting UV sensor application notion created a wireless UV sensor platform based on ZnO nanorods that send real-time gathered signals to a smartphone through Bluetooth. The sensor has a responsivity of 0.55 A/W, a response time of 3.1 s, and a recovery time of 1.25 s. A photo of the photocurrent measurement made with a smartphone is shown in Figure 2.4 (b) [46].

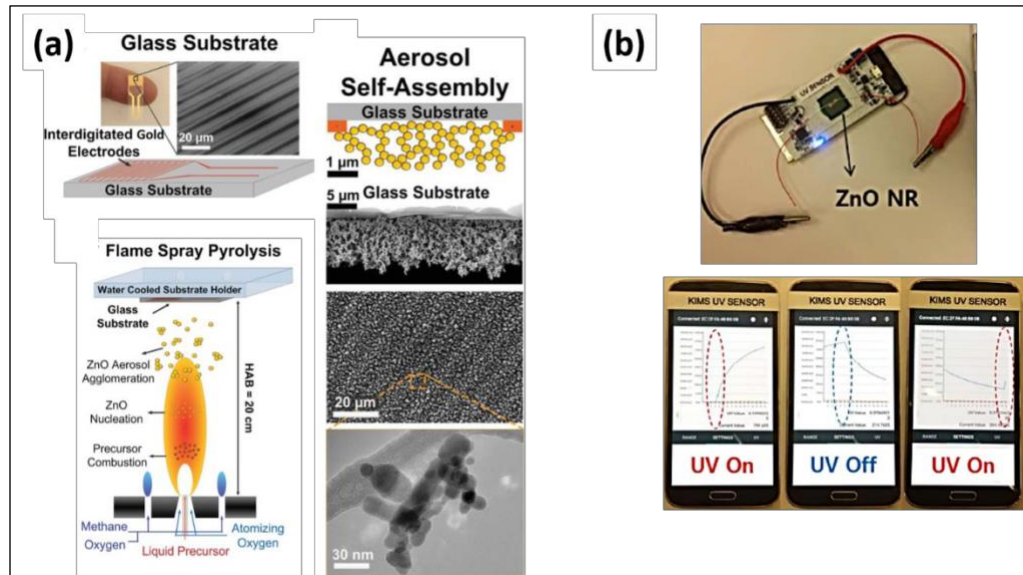


Figure 2.4 Shows (a) a schematic of a ZnO photodetector manufactured by flame spray pyrolysis and (b) a Photographic image of a ZnO UV sensor Bluetooth-connected to a smartphone displaying photocurrent variation during UV radiation on/off cycles [44].

Figure 2.5 shows how ZnO nanorod balls are created when seed solution nuclei aggregate and deposit on the fluorine-doped tin oxide (FTO) substrate's surface. Each aggregated seed acts as a location for nucleation. Renucleation and the following stages of the development process are shown in Figure 2.5 (b). Homogeneous nucleation precipitates in stage 1 create two rods, which are then connected to form a twinned nanorod. Stage 2 involves the formation of ZnO nanorods from the defect site in the main structure at the interface with the FTO substrate. In stage 3, the twinned nanorods' junction part is where the nanorods grow. Stage 4 results in a three-dimensional ball-shaped nanorod structure as succeeding nanorods develop in all directions [49]. A 3-D ZnO nanostructure is formed when individual nanorods of equal diameter and length are arranged in a circle. The bigger seed size used in the seed layer for the creation of 3-D ball

nanostructures lowers the supersaturation degree, limiting homogeneous nucleation and enabling heterogeneous nucleation. 20  $\mu\text{m}$  diameter 3-D ZnO nanorod balls are produced because of the growth rate being accelerated by heterogeneous nucleation. Ostwald ripening produces larger 3-D structures with wide gaps between them by causing smaller crystals to be consumed by larger crystals as they grow [50]. The development of 3-D structures reduces the system's overall surface energy, improving its energy efficiency [51]. According to energy-dispersive X-ray spectroscopy, ZnO nanoballs' atom ratio of Zn:O (0.9:1) is the same as the stoichiometric ZnO ratio [47].

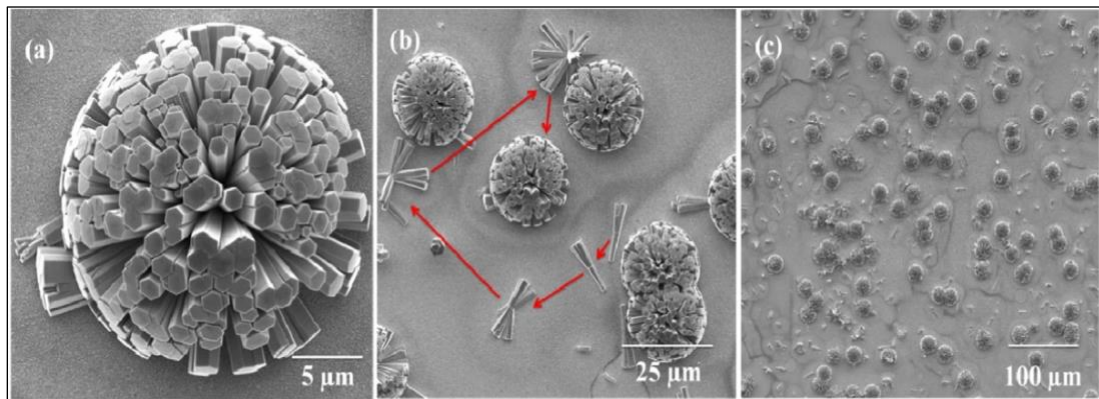


Figure 2.5 SEM images of the ZnO balls show, (a) ball-shaped nanorod structure in three dimensions as subsequent nanorods grow in all directions, (b) growth of newly generated nanorods along their own *c*-axis, as well as the nucleation and growth of rods from the joint section of the original structure, and (c) many ball-shaped nanorod structures [48].

## 2.2 Chemical Methods for Growing ZnO NSs

Several chemical processes have been used to create ZnO NSs, including the electrodeposition [44], sol-gel method [53-55], hydrothermal method [56-58], facile low-cost hydrothermal [57], chemical bath deposition [59, 60], simple solvothermal process [61], microwave synthesis [62, 63], facile low-temperature method [64], low-temperature

solution method [65], and laser-assisted chemical bath deposition (LACBD) technique [21, 23, 66]. All these techniques are utilized to grow ZnO nanorods, but LACBD is the simplest way because of its success, low cost, low temperature, environmental friendliness, and nontoxic nature. It is ecologically friendly and suitable for specific-area processing in industrial applications. In a two-step procedure, a buffer layer is first deposited on a glass substrate, and then a laser irradiation spot is used to produce ZnO micro/nanocrystals in a chemical bath that is an aqueous solution of a zinc precursor with additives to make it more stable.

According to Krajian et al.'s research, ZnO films can be created using the hydrothermal growth technique on ZnO seed layers that have already undergone RF magnetron sputtering. The structural, chemical, and physical characteristics of the produced films were studied based on the addition of zinc acetate and chloride salts. To verify the elemental stoichiometry of the hydrothermally produced ZnO film with low contamination, the morphology of nanostructures from hydrothermally grown ZnO films was examined by AFM, SEM, EDX, XRD, and XPS. Raman spectroscopy and FTIR characteristics, which confirmed the nanostructure growth with (002) preferred orientation and a hexagonal phase, were used to certify the texturization of the ZnO thick films produced by the hydrothermal growth method. The Raman and FTIR tests supported the XRD findings, which showed that the ZnO films had good quality, big grain size, and favored orientation [67].

Chou et al. [49] have proposed a facile low-cost hydrothermal method to control the growth of bridge semiconductor ZnO nanowires on laser-scribed graphene-based devices applied for NO gas discovery. The picosecond laser processing system was used to scribe graphene on glass substrates and to form V-shaped grooves. Throughout the

creation process of ZnO nanowires, the surfactant solution of methanol was added to the growth solution to decrease the surface tension of V-shaped grooves. Hence, the grown ZnO nanowires could increase their contact area from both sides of the groove edge. The investigational results showed that the V-shaped grooves of graphene on glass substrates were obtained by using optimal laser processing parameters including the pulse repetition rate of 300 kHz, scanning speed of 100 mm/s, laser fluence of 1.81 J/cm<sup>2</sup>, and the number of scribed passes of 3 times. Then, the ZnO nanowires were grown via the immersed processes of the seed layer solution for 80 min and the growth solution with a surfactant solution for 8 h. Consequently, the ZnO nanowires had the lowest electrical resistance of 453 Ω. Moreover, the sensitivities of gas sensors were approximately 14.7 %, 21.2 %, and 40.2 % when the ZnO nanowires were exposed to 50 ppm, 150 ppm, and 300 ppm NO gas, respectively.

The impact of the precursor chemistry on the properties of ZnO nanorods produced by the hydrothermal method described here has been researched by Yadav et al. The nanorods were created using RF-sputtered 50 nm ZnO seed layers over circuits that work with highly mismatched lattices of O<sub>2</sub>/p-Si substrates. Two zinc sources, zinc acetate, and zinc nitrate were simultaneously dissolved in a solvent (a solution of deionized water and hexamethylenetetramine) to produce the highly conducting, vertically aligned ZnO nanorods. The crystal structure and surface characteristics of NRs were investigated using X-ray diffraction and scanning electron microscope. The nanorods formed in the zinc acetate precursor solution were highly crystalline, sparsely packed, and had a clearly defined hexagonal top surface as compared to those made from zinc nitrate precursors. X-rays were employed to investigate the chemical composition of nanorods. An example of photoelectron spectroscopy is photoelectron resonance. The oxygen and zinc observed in

all the nanorods and the zinc acetate synthesized nanorods show high atomic percentages. The Ti/Au Ohmic contacts were deposited on top of ZnO nanorods to create a metal-semiconductor-metal (MSM) structure, which was used to study the electrical and photodetection properties of the material. Zero bias UV detection is demonstrated by the MSM structure built over the nanorods made from the zinc nitrate precursor, which has never been done before. The conducting qualities of the nanorods were assessed using the current-voltage characteristics of the MSM photosensor, and it was found that the NRs synthesized from zinc acetate were strongly conducting. The ability of the MSM photosensor to detect UV light from light-emitting diodes of comparable power but different wavelengths was tested. The ZnO NRs created in the zinc acetate precursor have extremely high photosensitivity [50].

ZnO is frequently manufactured using several techniques, according to Manthina et al. One of them is chemical bath deposition (CBD), which is both economical and advantageous for the environment due to the low temperatures employed. This study examines the many ZnO nanostructures that can be created using this technique. CBD is used to modify the formation of ZnO nanostructures using various additives and conditions, resulting in ZnO fibres, nanorods, cauliflower, nanorod balls, nanoforest, nanopencils, ellipsoids, and nanotubes. Research is being conducted on how these nanostructures might be used in a variety of technologies [47].

Zinc acetate was utilized as the starting material Guo et al. who created Zn-solutions using solvents and ligands with various boiling temperatures. On Si (100) substrates, ZnO thin films were produced by spin-coating. The effect of baking and boiling temperatures on the morphologies and orientation of the solvents and ligands was investigated. Solvents and ligands with high boiling points helped the mechanical stress

to relax and produce smooth ZnO thin films. Because low boiling temperature solvents and ligands were utilized to prepare Zn-solutions, the resulting ZnO thin films displayed a (002). The baking temperature was altered after creating Zn-solutions in n-propanol, 2-methoxy ethanol, 2-(methylamino) ethanol, and monoethanolamine (C<sub>2</sub>H<sub>7</sub>NO). Strongly (002)-oriented ZnO thin films were produced as a result [51].

Park et al. investigated a nickel oxide (NiO) and zinc oxide (ZnO) thin-film heterojunction photodiode made using a low-cost, energy-efficient sol-gel spin coating method. The extremely visible-transparent heterojunction photodiode with a smooth interface generates a good photoresponse and quantum efficiency when illuminated by UV light. A very good peak photoresponsivity of 21.8 A/W and external quantum efficiency (EQE) of 88 percent was achieved with a reverse bias of 5 V and an incoming light wavelength of 310 nm [52].

The synthesis of complex ZnO architectures with well-controlled morphology and an understanding of their growth mechanisms is required. In this study, a simple, low-temperature, chemical solution-based method was used to create a nano- or microstructure of ZnO in the form of balls. In situ cathodoluminescence, scanning electron microscopy, and energy dispersive spectroscopy were all employed to examine the morphological development of this unusual ball-shaped cluster. At the junction section of two primary one-dimensional ZnO nanorods, renucleation and sequential development of nanorods were observed. This discovery led to the self-assembly of intricate, three-dimensional ZnO hierarchical systems. We briefly looked at the mechanism of formation's inorganic additive Al (III) involvement in the precursor solution and structural faults in the growth process. The research's conclusions will help formulate a plan for creating micro-nanostructures with the appropriate geometric and functional properties [53].

The ZnO deposition process is carried out in a steel container called an autoclave using a hydrothermal technique [28], [54]. The autoclave container is expensive, and this is the method's biggest drawback. In comparison to the hydrothermal and sol-gel procedures, the chemical bath deposition approach is easier to utilize. Glassware can be utilized to cultivate NSs in this technique. However, chemical bath deposition also provides several benefits, including a cheap cost, easy methods, and low-temperature approaches in the range of 65 °C to 95 °C. Chemical bath deposition has also been utilized to synthesize NRs, nanowires, nano-cones, nanoparticles, and nanotubes, among other ZnO NSs. Chemical bath deposition is also a good way to synthesize NSs on a wide range of substrates, which might be beneficial in some commercial applications. Furthermore, the chemical bath deposition method regulates the properties of the as-grown structures by adjusting deposition temperature, duration, pH, substrate type, and precursor concentration.

Xu et al. have studied the optical material of a thin film, therefore, enhancing its optical quality using straightforward methods or techniques is a crucial research field. Using a sol-gel spin-coating technique, it was determined how the annealing temperature affected the microstructure and optical characteristics of ZnO thin films co-doped with Fe and Cl on glass substrates. According to the field emission scanning electron microscope, all samples had a double-layer structure, with single-crystal nanocolumns in the upper layer and polycrystalline nanoparticles in the lower layer. Some notable changes occur when the annealing temperature rises: the absorption edge is gradually redshifted; the UV emission gradually rises; and cavities gradually appear in the top layer of ZnO thin films. We are aware of only a few investigations into gaps in the lower layer of ZnO thin films. We think that mass transfer from the lower layer to the top layer is what causes the creation

of these holes. In other words, single crystal nanocolumns are created because of the sacrifice of polycrystalline nanoparticles in the lower layer of ZnO thin films [55].

Abd-Alghafour et al. created a UV detector based on zinc oxide (ZnO) thin film using the sol-gel method and zinc acetate dihydrate ( $\text{Zn}(\text{CH}_3\text{COO})_2 \cdot 2\text{H}_2\text{O}$ ) as a precursor. According to X-ray diffraction (XRD) patterns, the ZnO sample has a hexagonal crystal structure. Data from field emission scanning electron microscopy (FE-SEM) shows that the surface of the ZnO film is uniform, smooth, and has grains that are about 50 nm in size. With the use of photoluminescence spectroscopy (PL), near band-edge (NBE) and deep level-edge, PL emissions were identified as being respectively, broadband and near band-edge (NBE). The metal-semiconductor-metal (MSM) device based on the produced ZnO film displayed a sensitivity of 43 % and a response peak of 4.3 A/W when exposed to UV light, respectively, when exposed to light ( $0.66 \text{ W/cm}^2$ ) at 5 V. Under 380 nm light, the UV detector showed excellent time stability and robust photocurrent response. These findings demonstrate a low-cost approach for constructing a high-performance ZnO MSM UV photodetector with fast response, quick recovery, and high responsivities of graphene as a conductive layer to increase the performance of ZnO UV sensors is the most current approach. The advantage of graphene is that it has a high conductivity which prevents electron-hole pairs from recombination in the ZnO/graphene composite and transmittance over 97.7 % for single-layer graphene, which maximizes UV-light absorption, allowing for faster response and recovery times and higher photocurrent gain [56].

### 2.3 The Advantages of Using Hexamethylenetetramine (HMTA, C<sub>6</sub>H<sub>12</sub>N<sub>4</sub>)

Hexamethylenetetramine (HMTA, C<sub>6</sub>H<sub>12</sub>N<sub>4</sub>) was employed to form an OH<sup>-</sup> group ion via interaction with a water molecule. The OH<sup>-</sup> group is formed in two phases, the first is that HMTA creates NH<sub>3</sub> when it combines with water (H<sub>2</sub>O). The second reaction of NH<sub>3</sub> with water molecules is the formation of OH<sup>-</sup> group ions. When OH<sup>-</sup> interacts with Zn<sup>+2</sup>, Zn(OH)<sub>2</sub> and ZnO molecules are formed, which serve as the building blocks for the formation of ZnO NSs. The concentration of Zn(NO<sub>3</sub>)<sub>2</sub> · 6H<sub>2</sub>O and HMTA has a significant impact on the as-grown structure's properties. Adjusting the solution concentration in the initial phase of the deposition process can affect the characteristics of ZnO NSs. The mechanism of ZnO production in the LACBD approach may be characterized by using the Eqs. (2.1-2.4). The first and second equations show how HMTA reacts with H<sub>2</sub>O to create a basic environment by producing OH<sup>-</sup> ions. When OH<sup>-</sup> ions combine with Zn<sup>+2</sup> ions, Zn(OH)<sub>2</sub> is formed. ZnO is formed when OH<sup>-</sup> ions combine with Zn(OH)<sub>2</sub> and are then dehydrated to produce ZnO. It is important to note that the temperature of the reaction is critical to the breakdown of Zn(OH)<sub>2</sub> to produce ZnO [57], [58].



Moreover, hexamethylenetetramine (HMTA), which has been used to deliver OH<sup>-</sup> throughout the reaction processes one of the most used alkaline reagents. The synthesis process can be carried out at lower temperatures (100 °C) and atmospheric pressure when

HMTA is used. However, because of its advantage in manufacturing high-quality ZnO nanorods [59]. HMTA has several important roles to perform during the synthesis process. First, through thermal breakdown, HMTA provides the OH<sup>-</sup> ions that drive the precipitation reaction [60]. Second, by slowly releasing OH ions through heat degradation, HMTA acts as a pH buffer [61]. With an increase in pH, the rate of HMTA hydrolysis decreases, and vice versa. Third, HMTA binds to the nonpolar facets of ZnO nanorods, preventing Zn<sup>2+</sup> ions from accessing them, leaving only the polar (001) face available for epitaxial development [62][63].

#### **2.4 The Advantages of Using Zinc Acetate to Produce the ZnO**

The exceptional performance of nanostructured zinc oxide (ZnO) materials in electronics, optics, and photonics has piqued curiosity [83]. Wide bandgap semiconductor, luminescence characteristics, photoconductivity, and catalytic activity are only a few of the physical and chemical properties of ZnO [84]. Indeed, it has various advantages, including simplicity, low cost, environmentally friendly settings, and a wide range of versatility in terms of controlling the structure and morphology of the nanostructures generated by adjusting the deposition conditions. Most of the time, an aqueous solution is used for the deposition. The temperatures are therefore lower than the water's boiling point. Particularly ZnO, they have all been used to make semiconductor films.

Singh et al. have employed chemical approaches to synthesize nanostructured ZnO with various morphologies using several precursor solutions. The precursors have had a substantial impact on the shape of the zinc oxide. All nanorods with tapered ends, short-length rods with hexagonal prism geometry, and long-length rods with hexagonal prism

geometry with a proliferation of particle-like structures on the surface are found in a powder made from zinc chloride, zinc nitrate, and zinc acetate, respectively. The sensing performance of these powders was examined, and they discovered that the sensing response is influenced by surface shape. The zinc acetate-aided gas sensor produced the greatest performance against all the alcohols out of all the precursor solutions. As a result, zinc oxide produced from zinc acetate has been determined to have the best morphology for gas sensing applications [64].

Krajian et al. have studied zinc oxide (ZnO) nanowires prepared using a hydrothermal method. Three common salts utilized in synthesis are zinc nitrate hexahydrate, zinc acetate, and zinc chloride. Zinc acetate dihydrate is the most utilized in investigations, whereas zinc chloride is recommended for electrodeposition. In this study, the effects of time, temperature, solution concentration, and precursor chemical concentration ratios on the formation of ZnO nanowires are examined using zinc acetate dihydrate salt. The length of the nanowires is controlled by the growth time and solution concentration, whereas the diameter, is controlled by the precursor concentration ratio and solution concentration. Thin-film morphology is caused by high solution concentrations and high zinc acetate dihydrate concentrations. The usage of zinc acetate dihydrate as a zinc source for developing ZnO nanowires with a high aspect ratio has been found to have optimal growth characteristics (AR). Using zinc acetate dihydrate produces impurity-free ZnO nanowires, which eliminates the need for additional capping agents [54].

Akgun et al. investigated the use of zinc acetate dihydrate as a source of zinc cations to create ZnO hydrothermally. The same group looked at the impact of combining HMT with various zinc salts, including acetate, chloride, and nitrate, during the hydrothermal growth of ZnO nanowires. The outcomes showed that the largest aspect

ratio of ZnO nanowires could form with the zinc acetate dihydrate salt. A noticeable morphological impact on the resultant ZnO films was reported by [54] using various counterions of zinc in baths containing HMT. Acetate, formate, and chloride salts led to the formation of rod-like crystallites, whereas nitrate and perchlorate anions led to the formation of wires. Finally, flat hexagonal platelets were produced using sulfate anions. A comparison of the optical effects of various zinc salts with HMT during ZnO film hydrothermal growth is still missing [65].

Akgun et al. [66] have studied the hydrothermal method that is commonly used to make zinc oxide (ZnO) nanowires. Zinc acetate, zinc nitrate hexahydrate, sodium chloride, potassium chloride, and zinc chloride are three typical salts used in synthesis. Zinc nitrate hexahydrate is the most utilized in investigations, whereas zinc chloride is recommended for electrodeposition. In this study, the effects of time, temperature, solution concentration, and precursor chemical concentration ratios on the formation of ZnO nanowires are examined using zinc acetate dihydrate salt. The length of the nanowires is controlled by the growth time and solution concentration, whereas the diameter, is controlled by the precursor concentration ratio and solution concentration. Thin film morphology is caused by high solution concentrations and high zinc acetate dihydrate concentrations. The usage of zinc acetate dihydrate as a zinc source for developing ZnO nanowires with a high aspect ratio has been found to have optimal growth characteristics (AR). The use of zinc acetate dihydrate results in the creation of impurity-free ZnO nanowires, eliminating the requirement for additional capping agents [67]. During the hydrothermal growth of zinc oxide nanowires, the influence of several zinc salts as zinc sources was carefully examined. The temperature, pH, and transmittance of three separate zinc salt-prepared growth solutions were observed and used to provide a

broad explanation of the salt's effect. Microwave heating of the growth solutions was used in addition to the usual heating approach, and the differences in ZnO nanowires synthesized using both heating methods were investigated. It was discovered that ionization of zinc in growth solutions affects the creation of ZnO nanowires, resulting in growth with varying aspect ratios, and that synthesis of nanowires with the largest aspect ratio is possible with zinc acetate dihydrate salt.

The ZnO thin films that were produced using the sol-gel method on Si (100) and fused quartz glass substrates have been examined by Guo et al. On the (002) orientation and morphologies of ZnO thin films, the effects of baking temperature (170 °C - 350 °C), solution concentration (0.1 mol/L - 0.5 mol/L), and annealing temperature (250 °C - 400 °C) were investigated. The hydrolysis and heat breakdown of zinc acetate during baking could produce the ZnO nuclei. The most significant influence on the ZnO thin films (002) orientation came from the baking temperature. ZnO nuclei were formed when zinc acetate underwent simultaneous hydrolysis and thermal degradation while the wetting layer was baked at 210 °C, and the oriented attachment predominated in the creation of ZnO grains, resulting in the (002)-oriented ZnO nuclei. After further annealing at 250 °C for 60 minutes, the (002)-oriented ZnO thin film was formed because of the formation of the (002)-oriented ZnO nucleus. As the Zn-solution concentration and annealing temperature were increased, the ZnO grain size increased significantly. The highly (002)-oriented ZnO thin film was created by baking 0.4 mol/L Zn-solution at 210 °C for 10 minutes and annealing it at 400 °C for 60 minutes. The solid-state-directed aggregation of adjacent ZnO nuclei allows to production the highly (002)-oriented ZnO thin film at low temperatures. Table 2.2 shows the comparison of the LACBD technique with other techniques [51].